Elastic scattering of 96 MeV neutrons from iron, yttrium, and lead

A. Öhrn, J. Blomgren,* P. Andersson, A. Ataç, C. Gustavsson, J. Klug, P. Mermod, S. Pomp, P. Wolniewicz, and M. Österlund
Department of Neutron Research, Uppsala University, Box 525, S-75120 Uppsala, Sweden

L. Nilsson
Department of Neutron Research, Uppsala University, S-75120 Uppsala, Sweden and
The Svedberg Laboratory, Uppsala University, Uppsala, Sweden

B. Bergenwall
Department of Neutron Research, Uppsala University, S-75120 Uppsala, Sweden and
Department of Radiation Sciences, Uppsala University, Uppsala, Sweden

K. Elmgren and N. Olsson
Department of Neutron Research, Uppsala University, S-75120 Uppsala, Sweden and
Swedish Defence Research Agency (FOI), Stockholm, Sweden

U. Tippawan
Department of Neutron Research, Uppsala University, S-75120 Uppsala, Sweden and
Fast Neutron Research Facility, Chiang Mai University, Thailand

S. Dangtip and P. Phansuke
Fast Neutron Research Facility, Chiang Mai University, Thailand

P. Nadel-Turonski
Department of Radiation Sciences, Uppsala University, Uppsala, Sweden and
George Washington University, Washington, D.C., USA

O. Jonsson, A. Prokofiev, and P.-U. Renberg
The Svedberg Laboratory, Uppsala University, Uppsala, Sweden

V. Blideanu, C. Le Brun, J. F. Lecolley, F. R. Lecolley, M. Louvel, N. Marie-Noury, and C. Schweitzer
LPC, ISMRA et Université de Caen, CNRS/IN2P3, Caen, France

Ph. Eudes, F. Haddad, and C. Lebrun
SUBATECH, Université de Nantes, CNRS/IN2P3, Nantes, France

E. Bauge, J. P. Delaroche, M. Girod, and X. Ledoux
DPTA/SPN CEA, Bruyères-le-Châtel, France

K. Amos
School of Physics, University of Melbourne, Victoria 3010, Australia

S. Karataglidis
Department of Physics and Electronics, Rhodes University, Grahamstown, 6140, South Africa

R. Crespo
Departamento de Fisica, Instituto Superior Técnico, Lisboa, Portugal

W. Haider
Department of Physics, AMU, Aligarh, India
(Received 8 October 2007; published 11 February 2008)

Data on elastic scattering of 96 MeV neutrons from ^{56}Fe, ^{89}Y, and ^{208}Pb in the angular interval 10–70° are reported. The previously published data on ^{208}Pb have been extended, as a new method has been developed to obtain more information from data, namely to increase the number of angular bins at the most forward angles.

A study of the deviation of the zero-degree cross section from Wick's limit has been performed. It was shown that the data on ^{208}Pb are in agreement with Wick's limit while those on the lighter nuclei overshoot the limit significantly. The results are compared with modern optical model predictions, based on phenomenology and microscopic nuclear theory. The data on ^{56}Fe, ^{89}Y, and ^{208}Pb are in general in good agreement with the model predictions.

DOI: 10.1103/PhysRevC.77.024605 PACS number(s): 24.10.Ht, 25.40.Dn, 28.20.Cz

I. INTRODUCTION

The study of a system consisting of an incident nucleon interacting with a target nucleus requires the solution of a many-body equation. The system can, however, be approximated by considering two bodies interacting via a complex mean-field potential. This so-called optical model potential (OMP) is an important ingredient in calculations of cross sections, e.g., elastic and inelastic scattering, (p, n) and (n, p) reactions. In other words, a good global optical model is a powerful tool for predicting observables for energies and nuclides for which no measurements exist.

The optical models of today predict data successfully, but data are still needed for further developments. One commonly repeated request is neutron elastic scattering data at high energies [1]. The reason for this is that above 20 MeV very little high-quality neutron data exist. There are high-quality neutron total cross section data on a series of nuclei up to about 600 MeV [2]. In addition, (n, p) data in the forward angular range at modest excitation energies are available up to about 300 MeV for a rather large number of nuclei [3,4].

Apart from the extensive measurements of the *np* scattering cross section [5], there are very few measurements on neutron elastic scattering from nuclei heavier than $A = 6$. Above 30 MeV neutron energy, only three experiments have produced data with an energy resolution adequate for resolving individual nuclear states; an experiment at MSU at 30 and 40 MeV [6,7], one at UC Davis at 65 MeV [8,9] and one at LAMPF from 65 to 255 MeV [10]. Experiments at 55, 65, and 75 MeV have been performed at TIARA, Japan Atomic Energy Research Institute, and were published in Refs. [11,12], having energy resolutions in the 10–20 MeV range. Also available are a few measurements in the 0–30° range, between 80 and 350 MeV, all with energy resolutions of 15 MeV or more [13–17]. At small angles, this poor energy resolution is not a drawback, as elastic scattering dominates heavily. At larger angles, however, such a resolution makes data very difficult to interpret. An overview of the neutron elastic scattering experiments is given in Table I, where studied nuclei, neutron energies, energy resolutions and angular ranges are shown.

In the present paper, new data on elastic neutron scattering at 96 MeV from ^{56}Fe and ^{89}Y are published. They conclude a series of measurements to which the previously published data on ^{12}C, ^{16}O, and ^{208}Pb belong [18,19]. The analysis of the data on ^{208}Pb has been extended as part of this work and the results will be published here. A new method has been developed to extract more information from data, i.e., to increase the number of angular bins for the most forward angles. The reanalysis has not been performed for ^{12}C and ^{16}O as the angular distributions show little structure at small angles. The new data on ^{208}Pb supersedes those previously published.

Elastic neutron scattering at high energies is not only of academic interest, but has several applications in industry and medicine. One major application, which has attracted considerable interest lately, is the handling of nuclear waste by incineration in subcritical reactors fed by fast neutrons produced in spallation targets. New nuclear data are requested for feasibility assessments of these techniques. Four elements have attracted special interest; lead as spallation/cooling material, iron for shielding and construction, uranium as fuel and zirconium as fuel cladding. Our measurements cover three of these four requests. The deformed shape of the ^{238}U nucleus makes measurement of elastic neutron scattering difficult, mainly because of problems of resolving the ground state. In our experiments, we have used ^{89}Y instead of ^{90}Zr simply because the desired amount of ^{90}Zr was not possible to obtain. Instead of using natural zirconium, a monoisotopic target was preferred.

An interesting feature of the optical model is that it establishes a lower limit of the differential cross section at 0° if the total cross section is known, referred to as Wick's limit [20,21]. For a large range of energies and target masses, the zero-degree cross section falls very close to the limit. Therefore it has been suggested that this apparent equality could be used for normalization in lack of other methods [22]. The analysis of the previous data on ^{12}C [18] and an investigation of data from a previous experiment at 65 MeV [9] indicate, however, that the 0° cross sections can exceed Wick's limit significantly. After the publication of these two data sets, a theoretical study of this effect has been performed, see Ref. [23]. This has motivated a systematic study versus target mass, which is presented in Sec. IV C.

This paper is organized in the following way. A presentation of the neutron facility and the detector setup is given in Sec. II. The procedure of data reduction and discussion of the results are given in Secs. III and IV. Finally, a summary and conclusions are given in Sec. V.

II. EXPERIMENTAL ARRANGEMENT

A. Neutron beam and detector setup

The present experiments were performed at the The Svedberg Laboratory, Uppsala, Sweden. A detailed description of the neutron beam facility has been published in Ref. [24] and therefore only a brief summary will be given here.

*Corresponding author. Tel. +46 18 471 3788: jan.blomgren@tsl.uu.se

TABLE I. Neutron elastic scattering experiments with neutron energies $E_n \geqslant 30$ MeV.

Reference	Target	Energy (MeV)	Resolution (MeV at FWHM)	Angular range (°)
[6,7]	Ca, Si	30, 40	0.15	15–140
[11,12]	C, Si, Fe, Zr, Pb	55, 65, 75	10–20	2–57
[9]	C, Si, Ca, Fe, Sn, Pb	65	2.7	6–50
[13]	Al, Cu, Pb	84	30	2–25
[10]	C, Ca, Pb	65–225	4.5	7–23
[14]	Li, Be, C, Al, Cu, Cd, Pb, U	96	24	1–29
[15]	Li, Be, C, N, O, Al, Cu, Cd, Pb	136	27	0–20
[16]	C, Al, Cu, Cd, Pb	155	60	3–30
[17]	C, Al, Cu, Sn, Pb	350	15	1–20
[18,19]	C, O	96	3.7	10–70
Present experiment	Fe, Y, Pb	96	3.7	10–70

An overview of the facility is presented in Fig. 1. Neutrons of 96 MeV were produced by protons impinging on a neutron production target, consisting of lithium enriched to 99.98% in ^{7}Li, using the ^{7}Li(p, n) reaction. After the lithium target, the proton beam was bent into a well-shielded beam dump. The resulting neutron spectrum consisted of a peak at 96 ± 0.5 MeV (1.2 MeV FWHM) and a low-energy neutron tail, which was suppressed by time-of-flight techniques. The neutron beam was defined by a system of three collimators. At the scattering target, the beam diameter was 9 cm with a typical neutron yield of 2.5×10^6 s^{-1} over the whole beam area. The neutron beam was dumped in a tunnel about 10 m downstream of the experimental position. Neutron monitoring was performed by a fission counter (TFBC) and the integrated proton beam current from the proton beam dump.

The experimental setup SCANDAL (SCAttered Nucleon Detection AssembLy) was used to detect the scattered neutrons

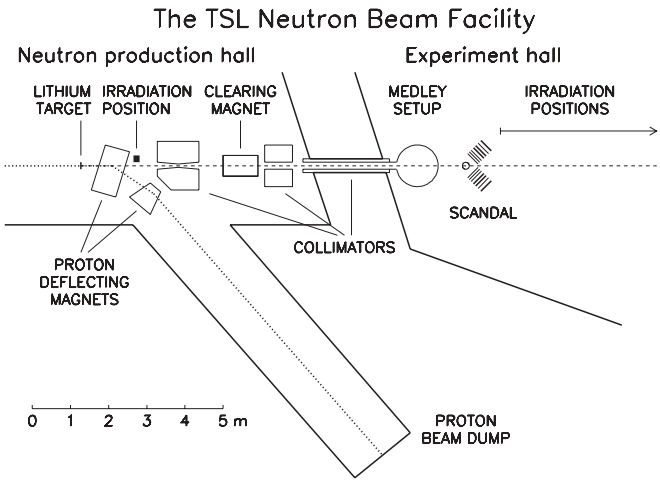

FIG. 1. Overview of the Uppsala neutron beam facility.

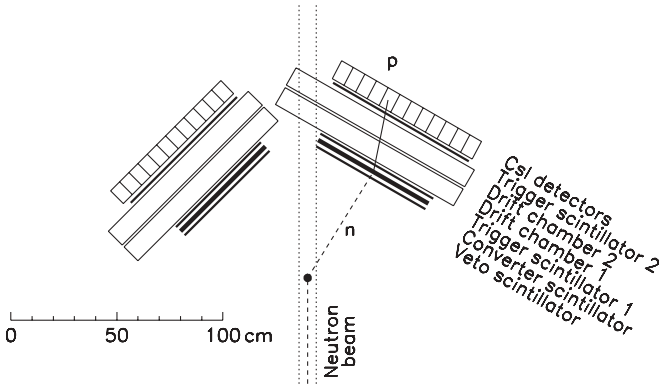

FIG. 2. Schematic layout of the SCANDAL setup. A typical event is indicated.

(see Fig. 2). The detection of neutrons is based on conversion to protons and detection of the recoil protons. The setup consists of two identical arms placed on each side of the beam, covering the angular ranges 10–50° and 30–70°. Each arm has a 2 mm thick veto scintillator for fast charged-particle rejection, a 10 mm thick neutron-proton converter scintillator, a 2 mm thick ΔE plastic scintillator for triggering, two drift chambers for proton tracking, another 2 mm thick ΔE plastic scintillator which is also part of the trigger, and an array of CsI detectors (12 on each arm) for energy determination of the recoil protons produced in the converter by *np* scattering. The trigger, when detecting neutrons, is defined by a coincidence of the two trigger scintillators, with the front detector acting as a veto. It is also possible to run SCANDAL in proton mode, by changing the veto detector to accept charged particles. The total energy resolution of the individual CsI crystals is different, and on average 3.7 MeV (FWHM), see Ref. [24].

B. Experimental procedure

The experiments were carried out in different runs of about one week each. Data on lead have previously been published in Ref. [18] where details about that particular experiment are given. Each experimental week begun with a calibration measurement in which a CH_2 target was placed in the neutron beam and recoil protons from *np* scattering were detected.

After calibration, the SCANDAL setup was changed to neutron detection mode in which the veto scintillator signals are used for charged-particle rejection. The lower limit of the angular range, 10°, represents an arm position where the scintillator detectors barely avoid being hit by the neutron beam. The largest angle, 70°, is the upper limit where it is possible to achieve reliable statistics in one week of data taking time. The overlapping angular range 30–50°, allows for the study of the consistency between the two arms. Four scattering targets were used, a natural iron cylinder (91.8% ^{56}Fe, 5.8% ^{54}Fe, 2.1% ^{57}Fe, and 0.3% ^{58}Fe), 5 cm high and 5 cm in diameter, with a mass of 777 g, an yttrium cylinder, 5.2 cm high, and 5 cm in diameter, with a mass of 456 g, a radiogenic lead cylinder (88% ^{208}Pb, 11% ^{206}Pb, and 1%

^{207}Pb), 6.3 cm high and 2.9 cm in diameter, with a mass of 444 g, and a carbon cylinder, 5 cm high, 5 cm in diameter, and with a mass of 178 g, which was used to provide data for normalization. Background data were recorded by removing the scattering cylinder from the setup.

The dead time in the data acquisition system varied with the different experiments. For iron, yttrium and lead, it was around 14%, 6%, and 4%, respectively, and for the background measurements about 2%.

III. DATA ANALYSIS

A. Calibration

The data were analyzed offline event-by-event using the ROOT package [25]. In a first stage, the time information from the drift chambers was converted to positions. The angular information and detector hit positions of the particle trajectories were calculated, based on the obtained drift chamber coordinates. It was required that the the calculated coordinates of the detected particle corresponded to a position within the volume between the trigger scintillators. The coordinates were also used to trace the trajectories of the protons, which in turn were used to establish the hit positions for the CsI detectors and the conversion points in the converter scintillator.

Each CsI detector was calibrated individually with *np* data from the calibration runs. Two calibration peaks in each CsI detector were identified; the pedestal channel corresponding to zero-energy deposition in the detector, and the *np* scattering peak. A linear relationship was assumed between pulse height (PH) and deposited energy. The energy of the *np* peak was obtained by calculating the energy loss of the proton through the detector setup from the target to the CsI in question. The centroid channel was determined by fitting a gaussian to the *np* peak.

Each plastic scintillator has two PM tubes attached to one of the longer horizontal sides. They were calibrated by choosing a narrow, central section of the scintillator, i.e., where the distance is approximately the same to both PM tubes and where it can be assumed that these detect half the light each of the deposited energy. Also for the plastic scintillators, the pedestal channel and the proton peak were used as calibration points. The total deposited energy of the plastic scintillators (ΔE) was obtained by adding the contribution from the two PM tubes. The shape of the plastic scintillators give rise to a geometric effect, i.e., protons with the same energy yield slightly different ΔE signals depending on where they hit the detector. The deviation from the expected ΔE value was mapped over the detectors as a function of the location in the scintillator, both horizontally and vertically, and could subsequently be compensated for.

To obtain the correct energy loss throughout the whole detector setup, the energy losses in materials where the proton is not detected, such as detector wrapping, drift chamber foils, drift chamber gas and air, were calculated.

Finally, the total energy of the charged particle was calculated as the sum of the different contributions from the detectors and other materials. This resulted in excitation-energy spectra for the different angles in the laboratory system related to the position of the CsI crystal in which the proton was stopped.

B. Data reduction

Protons were separated from other charged particles, mostly deuterons originating from the converter scintillator, by a ΔE-E technique. A two-dimensional cut was applied to a scatter plot where the sum of the detected energy losses in the two trigger scintillators was plotted versus the energies in the CsI detectors. Since the Q-value for ^{12}C(n, d) is -13.7 MeV, there is no physical background of deuterons in the energy range of elastic scattering and this cut is not crucial for the extraction of elastic scattering events.

To reject events from the low-energy tail of the neutron spectrum, a time-of-flight (TOF) cut was used. The TOF was defined as the time difference between the first trigger detector and a signal from the cyclotron radio frequency system. This information is, however, not important for the present experiment as a low-energy neutron in the beam cannot induce emission of a full-energy neutron from the scattering target.

In previous experiments using the SCANDAL setup, (see Refs. [19,24,26]), each CsI crystal defined an angular bin. For the present experiments, however, the CsI area for the crystals at the most forward angles, where the statistics allow such a procedure, has been divided into two areas to obtain more data points. This resulted in 36 angular bins for ^{56}Fe, 32 bins for ^{89}Y, and 30 for ^{208}Pb. The statistics were better for the iron experiment and therefore allowed more CsI detector hit areas to be split up.

To distinguish which events belonged to which bin, a scatter plot with the horizontal and vertical hit positions was constructed. In these scatter plots, two-dimensional cuts were applied in order to select the accepted hit area. Since the energy determination for events where a proton passes through more than one CsI detector is very poor, due to large straggling effects in CsI wrapping materials, it was important that the position cuts were set in such a way that the protons were completely stopped in a single detector.

Since the converter scintillator contains both carbon and hydrogen, neutrons can be converted to protons by the ^{12}C(n, p) reaction instead of the desired *np* scattering, i.e., H(n, p). The Q-value for the ^{12}C(n, p) reaction is -12.6 MeV meaning that at forward angles, an energy cut is sufficient to distinguish between the two reactions. At conversion angles larger than about 20°, the proton energies from the two processes overlap and it cannot be decided from which reaction the proton originates. Therefore, an opening angle criterion was set, demanding that the conversion angle be less than 10°. The procedure described above was also applied to the background data.

Up to this point, the data reduction was performed event-by-event. Subsequently, the data were stored in excitation-energy histograms, one for each angular bin. Background data were subtracted from the signal spectra after normalization to the same neutron fluence and taking dead time into consideration. The corresponding operations were also performed to produce

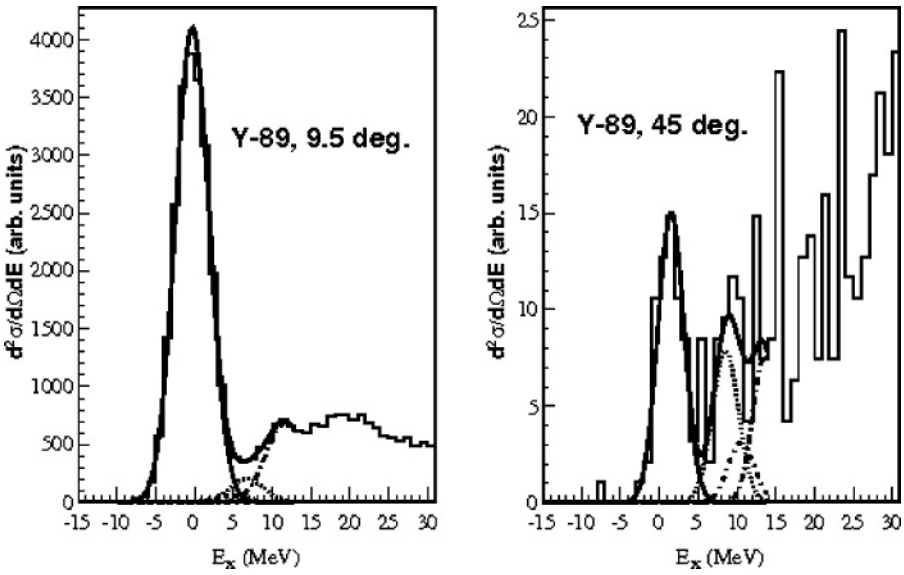

FIG. 3. Example of spectrum functions used to extract the number of elastic scattering events. The gaussian fitted to the ground state peak is solid. The gaussian at 7 MeV is dotted. The distribution of protons from ^{12}C(n, p) reactions in the converter is dash-dotted and the barely visible state at 5 MeV is dashed. The inelastic state at 9 MeV (only visible in the right panel) is described with a dash-dotted line. The sum of the contributions form the spectrum function drawn as a thick solid line. See the text for details.

variance histograms, to be used later for estimation of the statistical errors.

C. Extraction of elastic scattering events

To obtain the number of elastic scattering events at each angle, gaussians were fitted to the ground state peak and the lowest excited states, and subsequently, the area of the gaussians were calculated. An example of this is given in Fig. 3. The heights, positions, and widths of the ground state gaussians were treated as free parameters. The same width was used for the gaussians describing low-lying excited states, but the heights were allowed to vary independently. The centroids of the inelastic states were fixed relative to the ground state peak by the energy calibration. At excitation energies of about 10 MeV and up, protons from the ^{12}C(n, p) reaction in the converter formed a rather structureless distribution, approximated by a gaussian. The width and the height of the corresponding gaussian were treated as free parameters. Simultaneously, a spectrum function was constructed to describe the entire spectrum to 14 MeV above the ground state peak. The choice of which inelastic states to include was a rather pragmatic decision, based on visual inspection of the excitation spectra and by studying proton inelastic scattering at nearby energies, as well as neutron inelastic scattering at lower energies. For ^{56}Fe, a gaussian was fitted to the excited state at 4.5 MeV [27], and for ^{89}Y, gaussians were fitted to states at 5.0, 7.0, and 9.0 MeV [28].

The variance of the number of elastic scattering events was extracted by applying this method also to the variance histograms. At large angles, the fitting procedure described above could not be used due to poor statistics. For those angles, the ground state yield was extracted by integration, with limits determined by visual inspection.

D. Cross section calculation and normalization

The number of neutrons in the beam was given by either the fission counter (TFBC) or the integrated proton beam current. The number of target nuclei was calculated from the weight and volume of the scattering target. The solid angles for protons detected in the CsI crystals are individual for each crystal depending on the distance to the target and the size of the accepted detection area. A computer code was developed to calculate this, see Ref. [18]. The code also takes into account the neutron energy (which varies with neutron angle) as it will affect the conversion probability, due to the energy dependent np cross section. The result is individual effective solid angles for each CsI, containing the geometric solid angle and the probability that a converted proton hits the crystal.

The same code was used to calculate the average neutron scattering angle for each bin. Since the energy resolution is different for individual CsI crystals, the low-energy continuum originating from the ^{7}Li(p, n) reaction will contribute differently to the full-energy np peaks at different angles and hence to the ground state peaks in the excitation-energy spectra. This contribution, which is a function of the peak width [29] has been determined using experimental neutron spectra for the ^{7}Li(p, n) reaction measured by Byrd and Sailor [30]. Correction factors for this effect were used when calculating the cross section. The effect is typically around 3% and always less than 6%.

The proton detection efficiency has contributions from the efficiencies of each drift chamber plane, the efficiency of selecting the correct drift chamber wire in multiple-hit events and the CsI efficiency. The total drift chamber efficiency has been measured to 0.75 ± 0.10 (an average of 0.93 per plane). The efficiency of selecting the correct wire has been measured to 0.93 (0.98 per plane) and the CsI efficiency, i.e., the probability that a proton slowing down in the CsI crystal does not undergo a nuclear reaction before coming to rest, to 0.92 ± 0.01. This makes a total proton detection efficiency of 0.64 ± 0.10.

The absolute scale of the cross sections was given by the number of neutrons in the beam. The TFBC, however, has an uncertainty of more than 10% and therefore further normalization was required. The data on iron and yttrium were

measured relative to carbon. In Ref. [18] a new normalization procedure was introduced, using the known data on the total cross section and the reaction cross section, to calculate the total elastic cross section to which the elastic differential cross section was normalized. For carbon, the normalization uncertainty was estimated to 3%. Measuring relative to carbon has been adopted by us as a secondary standard for normalization of our data. We estimate the normalization procedure to have an uncertainty of about 5%.

Since extended targets have been used for the present experiments, corrections for neutron attenuation and multiple scattering were necessary. These corrections have been performed using a Monte Carlo code [31]. As input to the code, an angular distribution in the laboratory system was given, in this case the experimental data obtained with SCANDAL. After conversion to the c.m. system and calculation of the attenuation, the code simulated the experiment. The aim of the program was to find a distribution that, when used as input for the simulation, resulted in an output reproducing the measured angular distribution. For the new data set on ^{208}Pb this turned out not to be a good method as the angular distribution showed so prominent structure that the code could not successfully describe it. Instead a simulation of the experiment was carried out by an MCNPX [32] calculation, using the cross section predicted by the ENDF-VI/B library [33]. First, the code simulated elastic neutron scattering using a point target of ^{208}Pb. The second step was to simulate the reaction using a lead cylinder of the actual size of the experiment. The two angular distributions obtained were compared and correction factors could be calculated from the ratio of the two simulations. Finally, the data on ^{208}Pb were corrected for the content of ^{206}Pb.

E. Estimation of experimental uncertainties

A thorough investigation of the experimental uncertainties is described in Ref. [18] and therefore only an overview will be given here.

Since the purpose of the present experiment has been to obtain a set of relative differential cross section data, which is finally normalized using previously known information, only uncertainties that affect the shape of the angular distribution are of importance.

The random error is due to counting statistics and includes contributions from the background subtraction. It varies significantly with scattering angle, due to the steepness of the cross sections.

The Monte Carlo simulation for correction of multiple scattering, adds a statistical error to the point-to-point uncertainty. The total statistical errors, including both these contributions, are calculated in the program and given as output together with the corrected angular distribution. The results are listed in Tables II, III, and IV. In addition to the total errors, the relative statistical errors in the measurements, i.e., before corrections, are shown.

The correction (<6%) for the contribution from the low-energy continuum of the ^{7}Li(p, n) spectrum to the np scattering peak introduces a systematic uncertainty that varies with peak width and is therefore different for each CsI crystal due to their individual energy resolutions. Assuming a relative uncertainty of 10% in the correction, an error in the data of at most 0.6% arises.

For nuclei like ^{208}Pb which have a pronounced angular dependence for the elastic scattering differential cross section, small uncertainties in the angular information can produce significant uncertainties in the result. The effect is present also for iron and yttrium but is not as strong. The angular uncertainties in the present experiment are dominated by

TABLE II. Differential cross sections for elastic neutron scattering from ^{56}Fe at 96 MeV. The total statistical errors in the column "$\Delta d\sigma/d\Omega$" include random errors constituted by counting statistics and contributions from the multiple scattering corrections, while the column "Δrel." shows the relative statistical errors in the experiment, before these corrections are made. The columns "Δang." refer to cross section uncertainty due to the angle uncertainty in the measurement, as described in the text.

$\theta_{\text{c.m.}}$ (deg)	$d\sigma/d\Omega$ (mb/sr)	$\Delta d\sigma/d\Omega$ (mb/sr)	Δrel. (%)	Δang. (mb/sr)
9.5	4734	16	0.3	522
11.1	3461	16	0.4	436
12.9	2207	11	0.5	304
14.7	1167	8.7	0.7	208
17.1	420.4	4.3	0.8	89
18.5	275.9	4.8	1.2	42
21.0	130.8	3.1	1.2	5.0
22.6	121.3	3.3	1.4	2.0
24.8	112.8	3.3	1.8	0.5
25.3	143.6	3.2	1.5	1.0
25.9	105.3	2.8	1.9	1.5
26.7	108.0	2.6	1.8	2.5
28.4	110.5	2.6	1.9	9.0
29.2	80.9	1.7	1.8	5.5
29.6	84.2	2.1	2.1	5.5
30.8	68.1	1.9	2.3	2.5
32.2	47.9	1.7	2.8	4.5
33.6	40.2	1.6	2.9	3.0
33.6	36.9	1.5	3.0	3.0
35.2	21.0	1.1	3.6	5.0
37.3	15.7	0.8	2.7	1.0
37.6	13.4	1.0	3.9	0.8
39.2	14.1	1.0	4.2	0.8
41.5	10.3	0.6	3.7	0.1
42.3	7.8	0.7	6.2	0.3
43.5	6.4	0.6	7.1	0.3
46.0	10.7	0.5	4.3	0.3
47.0	4.9	0.4	7.5	0.4
50.2	4.9	0.4	6.4	0.3
51.0	3.7	0.4	7.2	0.2
54.4	1.3	0.3	8.6	0.1
54.6	2.3	0.4	8.1	0.1
58.6	1.0	0.3	16	0.04
62.6	0.65	0.22	31	0.05
66.6	1.0	0.2	16	0.04
70.6	0.48	0.13	21	0.01

TABLE III. Differential cross sections for elastic neutron scattering from ^{89}Y at 96 MeV. See Table II for details.

$\theta_{c.m.}$ (deg)	dσ/dΩ (mb/sr)	$\Delta d\sigma$/dΩ (mb/sr)	Δrel. (%)	Δang. (mb/sr)
9.5	5632	65	0.7	960
10.8	3478	45	0.8	750
13.0	1663	33	1.2	393
14.4	539.2	16	1.8	204
17.1	208.2	8.9	2.7	34
18.5	227.5	11.4	3.1	5.5
21.0	238.6	10.5	2.8	8.0
22.6	272.3	12.9	3.0	5.0
24.8	200.3	12.5	3.9	23
25.3	174.1	9.8	3.5	50
26.1	149.4	9.7	4.1	17
26.7	118.4	8.0	4.2	17
28.4	91.0	7.7	5.3	17.5
29.2	54.0	5.0	5.7	9.0
29.8	50.6	5.7	7.1	4.0
30.8	48.8	5.0	6.4	2.0
33.0	26.9	2.7	6.3	0.8
34.5	29.6	2.7	5.7	0.1
37.2	24.3	2.8	7.1	1.0
38.4	22.0	2.3	6.6	1.0
41.5	12.0	8.9	1.7	1.3
42.8	5.9	1.2	12.6	1.0
46.0	6.9	1.2	10.7	0.3
47.1	5.5	1.2	13.4	0.3
50.2	4.7	1.3	16.5	0.2
51.0	6.0	1.4	14.6	0.2
54.4	4.2	1.1	15.7	0.2
54.6	3.8	1.2	19.6	0.2
58.6	1.5	0.6	25	0.1
62.6	1.3	0.5	0.3	0.02
66.6	1.4	0.7	31.5	0.03
70.6	0.7	0.4	36.3	0.04

TABLE IV. Differential cross sections for elastic neutron scattering from ^{208}Pb at 96 MeV. See Table II for details.

$\theta_{c.m.}$ (deg)	dσ/dΩ (mb/sr)	$\Delta d\sigma$/dΩ (mb/sr)	Δrel. (%)	Δang. (mb/sr)
9.8	4396	47	1.0	1783
10.8	1792	28	1.3	869
13.0	961	28	1.9	89
14.4	623	18	2.1	88
17.2	640	15	2.1	34
18.5	787	16	2.0	89
21.0	287	10	3.1	82
22.5	282	13	3.7	39
24.8	171	12	5.0	4.0
25.3	119	8.3	5.3	9.8
25.9	132	12	5.0	7.3
26.7	103	7.1	5.8	4.5
29.5	128.6	5.3	3.6	11.4
30.0	109.6	4.1	3.5	12.6
33.4	52.1	3.4	5.3	10.7
34.4	34.4	2.7	6.0	4.7
37.6	29.6	2.4	6.8	1.0
38.7	26.3	2.2	7.4	0.2
41.9	18.7	2.0	9.3	3.1
43.2	18.3	1.9	8.9	2.8
46.3	7.6	1.3	12	0.2
47.2	8.6	1.3	12	0.1
50.3	5.9	1.0	15	0.4
51.0	8.8	1.3	13	0.6
54.6	3.4	0.9	22	0.5
54.9	3.5	0.7	18	0.6
59.3	2.0	0.7	26	0.1
63.6	1.0	0.5	43	0.2
67.2	0.5	0.4	66	0.1
71.2	0.7	0.5	52	0.1

the incomplete knowledge of the positions of the target and the drift chambers. Both these are known to slightly better than 1 mm, resulting in an angular uncertainty of about 1°. This uncertainty results in an equal shift of all data points produced by the same SCANDAL arm. The drift chambers contain, however, many drift cells, which work as physically independent detectors, each with its own TDC for time recording. Imperfect calibration can produce conversion position errors up to about 0.5 mm, which corresponds to about 0.5° shift of the presumed angle. This uncertainty is randomly distributed among the data points. The uncertainties are given in Tables II–IV.

IV. RESULTS AND DISCUSSION

A. Model predictions

Angular distributions of elastic neutron scattering from ^{56}Fe, ^{89}Y, and ^{208}Pb are presented in Fig. 4, where they are compared with phenomenological (left panel) and microscopic (right panel) optical model predictions. The theoretical curves have been folded with the experimental angular resolution to facilitate comparisons with data.

It is important to realize that the phenomenological and microscopic formed optical potentials are critically different, not only in their formulation but also in their intent. The phenomenological approach is a data driven formulation. Data are required in advance to define the parameter values of the potential. On the other hand, microscopically formed optical potentials are predetermined, and their success or not in reproducing measured data reflects on whatever inadequacies there may be in the underlying facets of their formulation.

Predictions by a phenomenological global optical model potential (OMP) of Koning-Delaroche [1] are given by the solid curves in the left panel of Fig. 4. This global OMP is valid for incident nucleon energies between 1 keV and 200 MeV and masses from 24 to 209. It is based on a smooth functional form for the energy dependence of the potential depths, and on physically constrained geometry parameters. An extensive collection of experimental data sets for different types of observables was used to determine the parameters of this OMP.

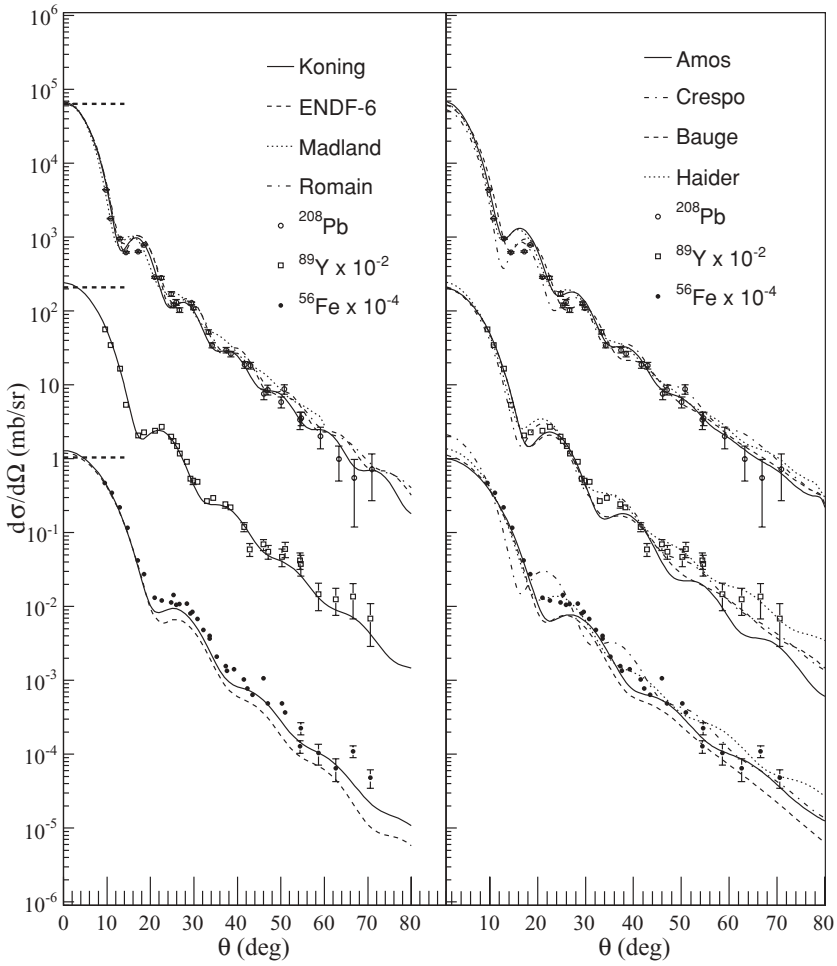

FIG. 4. Angular distributions of elastic neutron scattering from ^{56}Fe (closed circles), ^{89}Y (squares), and ^{208}Pb (open circles) at 96 MeV incident energy. Only statistical uncertanties are shown. The ^{56}Fe and ^{89}Y data have been multiplied with 10^{-4} and 10^{-2}, respectively. Left panel: predictions by phenomenological optical model potentials (OMP). The thick dotted horizontal lines show Wick's limit for the three nuclei. Right panel: predictions by microscopic OMP. The curves are identified in the text.

The dotted line in the left panel of Fig. 4 shows the result of a scattering calculation performed in 1990 by Kozack and Madland [34], using their global nucleon-nucleus intermediate-energy potential based on Dirac phenomenology for ^{208}Pb [35]. The potential contains scalar and vector terms, based upon the Walecka model [36], and includes isospin dependence through a relativistic generalization of the Lane model [37]. The isospin dependence was determined by simultaneous least-squares adjustment with respect to measured proton elastic scattering and neutron total cross section observables. Symmetrized Saxon-Wood form factors are used, and the potential contains a total of 20 parameters to describe nucleon scattering from ^{208}Pb in the energy range 95–300 MeV.

An OMP calculation by Romain and Delaroche [38], based on a dispersive OMP approach treating non-locality in a manner similar to that of Buck and Perey [39] for energy dependencies, is presented as the dash-dotted line in the left panel of Fig. 4.

Comparisons were also made with the cross sections given by the evaluated nuclear data files in the ENDF/B-VI library, Release 6 (ENDF-6) [33] and are presented with dashed curves in the left panel.

Amos *et al*. have developed a microscopic (g-folding) prescription for the optical potentials [40]. Therein an effective, medium dependent and complex *NN* interaction has been determined in coordinate space and mapped from g-matrices that are solutions of Brueckner-Bethe-Goldstone equations built upon the free Bonn-B *NN* interaction. This effective interaction is subsequently folded with microscopic model wave functions of the target to define a complex, fully nonlocal optical potential; the nonlocality arising from the nucleon exchange amplitudes due to the effects of the Pauli principle. The full nonlocal form of the Schrödinger equations are solved. While simple shell models have been used to define the ground state structures for ^{56}Fe and ^{89}Y, in the case of ^{208}Pb a Skyrme-Hartree-Fock model has been used in the folding process. This structure model, obtained with a constraint on the neutron equation of state giving a neutron skin $S = 0.16 \pm 0.02$ fm for ^{208}Pb, lead to g-folding predictions of 65 and 200 MeV proton and neutron scattering cross sections in excellent agreement with data [41]. The predictions are presented as the solid line in the right panel of Fig. 4.

Bauge, Delaroche, and Girod have developed a Lane-consistent, semimicroscopic OMP [43], which is built by folding radial matter densities from a Hartree-Fock-Bogoliubov calculation (using the Gogny D1S effective interaction) with an OMP in nuclear matter based on an extension of that of Jeukenne, Lejeune, and Mahaux (JLM) [46]. The result is presented as the dashed line in the right panel of Fig. 4.

This extended OMP features strong renormalizations of its isovector components, and has been tested extensively against (p, p) and (n, n) data, as well as (p, n) IAS data [43].

Haider and Saliem have developed a local microscopic optical potential [44], where the Bethe-Goldstone integral equation is solved using the soft-core Urbana v-14 inter-nucleon potential [45] to obtain the self-consistent nuclear matter optical potential as described in Ref. [46]. The radially dependent numerical g-matrices in different isospin states of the two-nucleon system are obtained as described in Refs. [44,47,48] and from this, the direct and exchange g-matrices for incident protons and neutrons are obtained. This was followed by folding the g-matrices over the point proton and neutron densities in the target to obtain the neutron-nucleus optical potential. In the present work [44], point proton and neutron densities obtained in the relativistic mean field approach have been used. The prediction is presented as a dotted line in the right panel in Fig. 4.

Finally, Crespo and Moro have made a prediction [49], illustrated by the dash-dotted line in the right panel, where the elastic observable was generated by a multiple scattering expansion of the optical potential in terms of the free NN transition amplitude, calculated in the single scattering, '$t\rho$', approximation [49]. In the description of the target nucleus, there is no distinction between protons and neutrons. For ^{56}Fe and ^{89}Y, the matter density distribution is given by a Fermi density distribution with parameters taken from Ref. [50]. In the case of ^{208}Pb, a two-parameter Fermi matter density distribution with half-density radius $c = 6.624$ fm and diffuseness $a = 0.549$ fm has been used.

B. Comparison with experimental data

The three data sets were compared with the results of the model predictions described above. The reduced χ^2 (from now on called χ^2) was calculated to investigate the agreement between theory and data. As a normalization error could produce a major χ^2 contribution, it was also tested to renormalize all theory models to produce a minimum χ^2. It should be noted that none of the predictions contain parameters adjusted to the present experiment.

Visual inspection of the ^{56}Fe data and theory predictions shows that all models except Crespo-Moro describe the shape of the experimental angular distribution reasonably well. χ^2 values were calculated and the results were 9 for Haider-Saliem, 20 for Koning-Delaroche, 36 for Amos *et al*., 46 for Bauge *et al*., and 57 for ENDF-6. For the renormalization test, the four data points at the angles 21.0°, 22.6°, 24.8°, and 25.3° were removed. The reason for this is that these data points are in the first minimum, where the formal errors are small, but there are unknown systematic errors due to the multiple scattering correction which we believe are large. If not removed for the renormalization test, they will dominate the calculation. With renormalization, all χ^2 values were lowered significantly. Haider-Saliem required least renormalization (0.95) resulting in a slightly improved χ^2, but still around 9. Koning-Delaroche required a renormalization of 1.20 resulting in a χ^2 value of 4. The lowest χ^2 was obtained for Amos *et al*. (3.5) with a fairly large renormalization (1.30). The other models require about 25–40 % renormalization with optimum χ^2 values between 5 and 10. All models, except Haider-Saliem, predict a deep first minimum in the angular distribution.

The theory predictions describe the shape of the measured angular distribution of ^{89}Y well. The lowest χ^2 value (1.5) is obtained for the Koning-Delaroche model and for the other models a χ^2 around 5 is obtained. Renormalization produces χ^2 values that are slightly lower. The Koning-Delaroche prediction has a χ^2 value of 1.1 for 1.08 renormalization, while the other models produce χ^2 values around 3. Amos *et al*. and Bauge *et al*. require for optimum χ^2 0.80 renormalization, while Crespo-Moro and Haider-Saliem require renormalization of 0.98 and 0.82, respectively.

Comparison of the ^{208}Pb data with the model predictions, shows that the models are in reasonably good agreement with the experimental data. Calculations of χ^2 give resulting values around 3 for Bauge *et al*., ENDF-6, Koning-Delaroche, and Romain *et al*. around 7 for Amos *et al*. and Crespo-Moro, and around 12 and 16 for Madland-Kozack and Haider-Saliem, respectively. For the renormalization test, three data points at 13.0°, 14.4°, and 17.2° were removed. These data points represent the first minimum of the angular distribution. The formal errors are small in this region, but there are unknown systematical errors due to the multiple scattering correction, which we believe are large. Renormalization reduces the χ^2 value for all models, with none exceeding 5. Bauge *et al*. and Koning-Delaroche required 0.97 renormalization, ENDF-6 and Romain *et al*. 0.93 and the other models 0.75–0.85.

C. Wick's limit

A basic feature of the optical model is that it establishes a lower limit on the differential elastic scattering cross section at 0° if the total cross section is known. This is often referred to as Wick's limit [20,21],

$$\frac{d\sigma(0^\circ)}{d\Omega} \geqslant \left(\frac{\sigma_T}{4\pi\lambda\!\!\!^{-}}\right)^2.$$

For most neutron scattering experiments below 30 MeV, it has been found that the zero-degree cross section is very close to the limit [51,52] and in the absence of a good experimental normalization this has lead to the suggestion that Wick's limit should be treated as an equality [22]. There is, however, no *a priori* reason why the 0° cross section cannot exceed the limit significantly, which has also been studied in Ref. [23]. Optical model calculations using the model of Koning-Delaroche have been performed for various nuclei and energies. From those data, the deviation from Wick's limit has been calculated. It was found that over a wide range of incident energies and target masses, the deviations of the zero-degree differential cross section from Wick's limit are small, at most a few percent. For ^{208}Pb this range is 4–80 MeV while the corresponding range for ^{89}Y is 10–60 MeV. The range becomes more narrow, the lighter the nucleus. There is, however, for all nuclei a wide energy range over which the deviation from Wick's limit does not exceed a few percent, while below and above this range the deviations are significant.

TABLE V. Wick's limit, $(\sigma_T/4\pi\lambda\!\!\!^{-})^2$, with an error of at most 1% coming from the determination of the total cross section, and the differential cross sections at 0°. The error for the extrapolated cross section at 0° contains contributions from the normalization procedure and the standard deviation of the calculated average value of the extrapolated cross section at 0°. Predictions from Refs. [23,53] are also tabulated.

Nucleus	Wick's limit	$d\sigma(0^\circ)/d\Omega$	Ratio (present data/Wick's limit)	Pred. by [23,53]
^{12}C	0.77	1.3 ± 0.13	1.70 ± 0.17	–
^{16}O	1.30	2.0 ± 0.2	1.54 ± 0.15	–
^{56}Fe	10.4	12.0 ± 1.3	1.14 ± 0.12	1.22
^{89}Y	20.9	22.7 ± 2.2	1.09 ± 0.10	1.13
^{208}Pb	63.7	60 ± 14	0.95 ± 0.22	1.03

In our previous measurement [18], the data on ^{208}Pb was in good agreement with Wick's limit while the ^{12}C data overshoot the limit with about 70%. Investigations of the zero-degree cross section for ^{16}O [19], ^{56}Fe, and ^{89}Y show that the data exceed Wick's limit with 54%, 14%, and 9%, respectively (see Table V). Since our measurements do not reach 0°, extrapolations using the various models described above (except for the Crespo-Moro model), have been used to determine the cross section at 0°. The theory models have been normalized to our data set, so that their predicted cross section at the lowest measured angles coincide with our measured values. The average value at 0° of all model extrapolations has been adopted for the Wick's limit comparison. The estimated error has been determined to about 10%, with contributions from the normalization procedure with a 3% uncertainty (see Ref. [18]), and the standard deviation of the calculated average value.

Deviations from equality have also been observed in the neutron scattering experiments at 65 MeV [9] and at 65–225 MeV [10], although not explicitly pointed out by the authors. Based on the information in the publication from the 65 MeV experiment [9], we conclude that the C data lie about 30% above the limit, the data on Si, Ca about 10% above whereas Sn and Pb agree with the limit. From the experiment at 65–225 MeV [10], we conclude that the data on Ca are about 10% above the limit at 65 MeV and the deviation grows larger with increasing energy to reach about 100% deviation from the limit at 225 MeV. The Pb data are in agreement with the limit up to about 130 MeV. At the higher energies, the extrapolated data at 0° are about 10% above the limit. Comparison with Ref. [23] corroborates these results. The extrapolated cross sections at 0° for the C measurements [10] are, however, below our result and the result we obtained when studying Ref. [9].

V. SUMMARY, CONCLUSIONS, AND OUTLOOK

We report differential cross sections of elastic scattering of 96 MeV neutrons from ^{56}Fe, ^{89}Y, and ^{208}Pb. The ^{208}Pb data, previously published in Ref. [18], have been reanalyzed, resulting in additional angular bins at forward angles, where the cross section is very steep. The new data set supersedes the old one. The overall agreement for ^{56}Fe, ^{89}Y, and ^{208}Pb with predictions from theoretical models, both phenomenological and microscopic, is reasonably good. These measurements provide important input to the development of optical models, not the least because of the scarcity of elastic neutron scattering data above 20 MeV.

A study of the deviation from Wick's limit has been performed. The extrapolated 0° cross section for ^{208}Pb is in agreement with the limit, but large deviations have been found for the lighter nuclei we have studied. These results show the same trend as the previous neutron scattering experiments at 65 MeV [9] and 65–225 MeV [10], and are in agreement with predictions in a recently published paper [23].

The SCANDAL setup is being upgraded with thicker CsI crystals, which will allow for measurements at higher energies, i.e., up to 175 MeV which is the maximum energy that can be delivered at the neutron beam facility at the The Svedberg Laboratory (TSL). Data at this energy will certainly be beneficial for the future development of optical models [1].

The isovector term in optical models can be determined from neutron and proton elastic scattering data if the data are obtained at the same energy and if they range over a series of nuclei. Data on elastic proton scattering exist already in literature and together with the present data set on elastic neutron scattering, a determination of the isovector term should be possible. Such an investigation is underway.

ACKNOWLEDGMENTS

We wish to thank the technical staff of the The Svedberg Laboratory for enthusiastic and skillful assistance. This work was supported by Barsebäck Power AB, Forsmark AB, Ringhals AB, the Swedish Nuclear Power Inspectorate, the Swedish Nuclear Fuel and Waste Management, the Swedish Defense Research Agency, the European Council, and the Swedish Research Council.

[1] A. J. Koning and J. P. Delaroche, Nucl. Phys. **A713**, 231 (2003).
[2] R. W. Finlay, W. P. Abfalterer, G. Fink, E. Montei, T. Adami, P. W. Lisowski, G. L. Morgan, and R. C. Haight, Phys. Rev. C **47**, 237 (1993).
[3] J. Rapaport and E. Sugarbaker, Annu. Rev. Nucl. Part. Sci. **44**, 109 (1994).
[4] W. P. Alford and B. M. Spicer, Adv. Nucl. Phys. **24**, 1 (1998).
[5] V. G. J. Stoks, R. A. M. Klomp, M. C. M. Rentmeester, and J. J. de Swart, Phys. Rev. C **48**, 792 (1993).
[6] R. P. DeVito, S. M. Austin, W. Sterrenburg, and U. E. P. Berg, Phys. Rev. Lett. **47**, 628 (1981).
[7] R. P. DeVito, S. M. Austin, U. E. P. Berg, R. De Leo, and W. A. Sterrenburg, Phys. Rev. C **28**, 2530 (1983).
[8] F. P. Brady, T. D. Ford, G. A. Needham, J. L. Romero, C. M. Castaneda, and M. L. Webb, Nucl. Instrum. Methods A **228**, 89 (1984).

[9] E. L. Hjort, F. P. Brady, J. L. Romero, J. R. Drummond, D. S. Sorenson, J. H. Osborne, B. McEachern, and L. F. Hansen, Phys. Rev. C **50**, 275 (1994).
[10] J. H. Osborne, F. P. Brady, J. L. Romero, J. L. Ullman, D. S. Sorensson, A. Ling, N. S. P. King, R. C. Haight, J. Rapaport, R. W. Finlay, E. Bauge, J. P. Delaroche, and A. J. Koning, Phys. Rev. C **70**, 054613 (2004).
[11] M. Ibaraki, M. Baba, T. Miura, Y. Nauchi, Y. Hirasawa, N. Hirakawa, H. Nakashima, S. Meigo, O. Iwamoto, and S. Tanaka, J. Nucl. Sci. Technol., Suppl. **1**, 683 (2000).
[12] M. Baba, M. Ibaraki, T. Miura, T. Aoki, Y. Hirasawa, H. Nakashima, S. Meigo, and S. Tanaka, J. Nucl. Sci. Technol., Suppl. **2**, 204 (2002).
[13] A. Bratenahl, S. Fernbach, R. H. Hildebrand, C. E. Leith, and B. J. Moyer, Phys. Rev. **77**, 597 (1950).
[14] G. L. Salmon, Nucl. Phys. **21**, 15 (1960).
[15] C. P. van Zyl, R. G. P. Voss, and R. Wilson, Philos. Mag. **1**, 1003 (1956).
[16] R. S. Harding, Phys. Rev. **111**, 1164 (1958).
[17] A. Ashmore, D. S. Mather, and S. K. Sen, Proc. Phys. Soc. A **71**, 552 (1958).
[18] J. Klug, J. Blomgren, A. Ataç, B. Bergenwall, A. Hildebrand, C. Johansson, P. Mermod, L. Nilsson, S. Pomp, U. Tippawan, K. Elmgren, N. Olsson, O. Jonsson, A. V. Prokofiev, P.-U. Renberg, P. Nadel-Turonski, S. Dangtip, P. Phansuke, M. Österlund, C. Le Brun, J. F. Lecolley, F. R. Lecolley, M. Louvel, N. Marie-Noury, C. Schweitzer, Ph. Eudes, F. Haddad, C. Lebrun, A. J. Koning, and X. Ledoux, Phys. Rev. C **68**, 064605 (2003).
[19] P. Mermod, J. Blomgren, C. Johansson, A. Ohrn, M. Osterlund, S. Pomp, B. Bergenwall, J. Klug, L. Nilsson, N. Olsson, U. Tippawan, P. Nadel-Turonski, O. Jonsson, A. Prokofiev, P.-U. Renberg, Y. Maeda, H. Sakai, A. Tamii, K. Amos, R. Crespo, and A. Moro, Phys. Rev. C **74**, 054002 (2006).
[20] G. C. Wick, Atti. R. Accad. Naz. Lincei, Mem. Cl. Sci. Fis. Mat. Nat. **13**, 1203 (1943).
[21] G. C. Wick, Phys. Rev. **75**, 1459 (1949).
[22] P. E. Hodgson, *The Optical Model of Elastic Scattering* (Oxford University Press, Oxford, 1963), p. 34.
[23] F. S. Dietrich, J. D. Anderson, R. W. Bauer, and S. M. Grimes, Phys. Rev. C **68**, 064608 (2003).
[24] J. Klug, J. Blomgren, A. Ataç, B. Bergenwall, S. Dangtip, K. Elmgren, C. Johansson, N. Olsson, S. Pomp, A. V. Prokofiev, J. Rahm, U. Tippawan, O. Jonsson, L. Nilsson, P.-U. Renberg, P. Nadel-Turonski, A. Ringbom, A. Oberstedt, F. Tovesson, V. Blideanu, C. Le Brun, J. F. Lecolley, F. R. Lecolley, M. Louvel, N. Marie, C. Schweitzer, C. Varignon, Ph. Eudes, F. Haddad, M. Kerveno, T. Kirchner, C. Lebrun, L. Stuttgé, I. Slypen, A. Smirnov, R. Michel, S. Neumann, and U. Herpers, Nucl. Instrum. Methods A **489**, 282 (2002).
[25] http://root.cern.ch
[26] C. Johansson, J. Blomgren, A. Ataç, B. Bergenwall, S. Dangtip, K. Elmgren, A. Hildebrand, O. Jonsson, J. Klug, P. Mermod, P. Nadel-Turonski, L. Nilsson, N. Olsson, S. Pomp, A. V. Prokofiev, P.-U. Renberg, U. Tippawan, and M. Österlund, Phys. Rev. C **71**, 024002 (2005).
[27] N. Olsson, E. Ramström, and B. Trostell, Nucl. Phys. **A513**, 205 (1990).
[28] N. Marty, M. Morlet, A. Willis, V. Comparat, and R. Frascaria, Nucl. Phys. **A238**, 93 (1975).
[29] J. Rahm, J. Blomgren, H. Condé, S. Dangtip, K. Elmgren, N. Olsson, T. Rönnqvist, R. Zorro, A. Ringbom, G. Tibell, O. Jonsson, L. Nilsson, P.-U. Renberg, T. E. O. Ericson, and B. Loiseau, Phys. Rev. C **57**, 1077 (1998).
[30] R. C. Byrd and W. C. Sailor, Nucl. Instrum. Methods A **264**, 494 (1989).
[31] B. Holmqvist, B. Gustavsson, and T. Wiedling, Ark. Fys. **34**, 481 (1967); later updates by N. Olsson.
[32] http://mcnp-green.lanl.gov/index.html, L. S. Waters, MCNPX Users' Manual—Version 2.1.5, Los Alamos National Laboratory, November 14, 1999.
[33] P. F. Rose and C. L. Dunford, ENDF-102: Data Formats and Procedures for the Evaluated Nuclear Data File ENDF-6, Technical Report BNL-NCS-44945 (Brookhaven National Laboratory, National Nuclear Data Center, Upton, NY, 1991); V. McLane, ENDF201: ENDF/B-VI Summary Documentation, Technical Report BNL-NCS-17541, 4th ed., Suppl. 1 (Brookhaven National Laboratory, National Nuclear Data Center, Upton, NY, 1996);for internet access see www.nndc.bnl.gov.
[34] R. Kozack and D. G. Madland, Nucl. Phys. **A509**, 664 (1990).
[35] R. Kozack and D. G. Madland, Phys. Rev. C **39**, 1461 (1989).
[36] B. D. Serot and J. D. Walecka, Adv. Nucl. Phys. **16**, 1 (1986).
[37] A. M. Lane, Nucl. Phys. **35**, 676 (1962).
[38] P. Romain and J. P. Delaroche, *Proceedings of a Specialists Meeting* (OECD, Paris, 1997) (http://db.nea.fr/html/science/om200/), p. 167.
[39] F. Perey and B. Buck, Nucl. Phys. **32**, 353 (1962).
[40] K. Amos, P. J. Dortmans, H. V. von Geramb, S. Karataglidis, and J. Raynal, Adv. Nucl. Phys. **25**, 275 (2000).
[41] S. Karataglidis, K. Amos, B. A. Brown, and P. K. Deb, Phys. Rev. C **65**, 044306 (2002).
[42] R. Machleidt, Adv. Nucl. Phys. **19**, 189 (1989).
[43] E. Bauge, J. P. Delaroche, and M. Girod, Phys. Rev. C **63**, 024607 (2001).
[44] S. M. Saliem and W. Haider, J. Phys. G **28**, 1313 (2002).
[45] I. E. Lagaris and V. R. Pandharipande, Nucl. Phys. **A359**, 331 (1981).
[46] J. P. Jeukenne, A. Lejeune, and C. Mahaux, Phys. Rev. C **16**, 80 (1977).
[47] B. A. Brieva and J. R. Rook, Nucl. Phys. **A291**, 299 (1977); **A291**, 317 (1977); **A297**, 206 (1978); **A307**, 493 (1978).
[48] N. Yamaguchi, S. Nagata, and J. Matsuda, Prog. Theor. Phys. **70**, 459 (1983); **76**, 1289 (1986).
[49] R. Crespo, R. C. Johnson, and J. A. Tostevin, Phys. Rev. C **46**, 279 (1992).
[50] R. C. Barret and D. F. Jackson, *Nuclear Sizes and Structure* (Clarendon Press, Oxford, 1979), ISBN 0198512724.
[51] N. Olsson, B. Trostell, E. Ramström, B. Holmqvist, and F. S. Dietrich, Nucl. Phys. **A472**, 237 (1987).
[52] J. H. Coon, R. W. Davis, H. E. Felthauser, and D. B. Nicodemus, Phys. Rev. **111**, 250 (1958).
[53] F. S. Dietrich, private communication (2007).